A possible long-term and very-deep aseismic slip event activating seismicity off Tohoku

F. Tomita[1]

[1]International Research Institute of Disaster Science, Tohoku University, 468-1 Aramaki-Aza-Aoba, Aoba-ku, Sendai, 980-8572, Japan.

Corresponding author: Fumiaki Tomita (fumiaki.tomita.d8@tohoku.ac.jp)

Key Points:

- GNSS observations suggest a possible long-term aseismic slip event since late 2019 off Tohoku.
- The long-term aseismic slip event is located at the deep plate interface, which is same or deeper than the similar event since 2002.
- The repeated ocuurence of the aseismic slip events may activate seismicity at the shallower plate interface.

Abstract

Various slips at plate interfaces in subduction zones have been documented, and the role of aseismic slips in strain release and stress re-distribution has been revealed. Prior to the M9 2011 Tohoku earthquake in Japan, various small-scale aseismic slip events which possibly affected the occurrence of the 2011 Tohoku earthquake had been reported. However, the small-scale aseismic slip behaviors after the M9 2011 Tohoku earthquake have not been well-clarified because the dominant postseismic deformation of the 2011 Tohoku earthquake has hidden minor aseismic slips. In this study, we performed trajectory models for the GNSS time-series after eliminating the postseismic deformation of the 2011 Tohoku earthquake, and we extracted afterslips followed by M7 class earthquakes, and an ongoing long-term aseismic slip event (L-ASE) since late 2019. The spatial extent of these aseismic slips was also clarified, and the 2019 L-ASE was estimated to be in the down-dip area of the seismogenic zone. As a similar L-ASE was also found before the 2011 Tohoku earthquake, a comparison of these L-ASEs suggests that the repeated L-ASEs promoted strain accumulation in the shallow plate interface, including the M9 rupture area, and may be markers preceding M7 class seismicity. Because L-ASEs are key phenomena in assessing sequential seismic behaviors in the Tohoku subduction zone, monitoring the ongoing L-ASE and investigating its physical interaction with other slip behaviors is important.

Plain Language Summary

Along a plate interface in a subduction zone, we can find various types of slip behaviors, such as various magnitudes of interplate earthquakes, afterslip, slow earthquakes, slow slip event, fault coupling, creeping, and so on. Recently, the role of aseismic slips has been noted because they show notable interaction with the other slip phenomena. In the Tohoku subduction zone, Japan, where the 2011 M9 Tohoku earthquake occurred, a long-term aseismic slip event (L-ASE) was found prior to 2011 and was considered to be one of the precursor of the M9 earthquake. This study newly found a similar L-ASE at the deep plate interface since late 2019 by elaborated GNSS time-series processing techniques. The 2019 L-ASE would be a recurring event of the previous L-ASE. From the comparison of these L-ASE, possible senarios suggesting interection between the L-ASEs and the other slip phenomena was discussed, and then the L-ASEs may bring about M7-class seismicity and provide strain accumulation in the M9 rupture area. Since the 2019 L-ASE may be still ongoing, monitoring of this event and investigation of its physical role through numerical simulation will be important to assess the hazard risk off Tohoku in the future.

1 Introduction

Various slip behaviors have been documented along plate interfaces, such as interplate earthquakes (e.g., Suito et al., 2011; Iinuma et al., 2011), afterslip (e.g., Suito et al., 2011; Iinuma et al., 2016), slow-slip events (SSEs) (e.g., Schwartz & Rokosky, 2007), and slow earthquakes (e.g., Schwartz & Rokosky, 2007; Obara & Kato, 2016; Nishikawa et al., 2019). SSEs have various characteristics, including regular SSEs (e.g., Hirose et al., 2011) and SSEs accompanying earthquake swarms (e.g., Villegas-Lanza et al., 2015; Uchida et al., 2016; Nishikawa et al., 2019). Moreover, long-term (decadal) aseismic slip events (L-ASEs), which may be considered as a temporal decrease in the interplate coupling, have been reported (Yokota & Koketsu, 2015;

Mavrommatis et al., 2015; Tsang et al., 2015). The diversity of slip behaviors suggests a spatial variation in frictional properties (e.g., Miyazaki et al., 2004; Nakata et al., 2012). Slip behaviors are quite different among subduction zones (Nishikawa et al., 2019); thus, compiling slip phenomena in subduction zones is important to assess frictional properties and future seismic hazard (Nakata et al., 2016; Nishikawa et al., 2023).

The Tohoku subduction zone along Japan Trench has experienced various slips, such as the 2011 M_w9.0 Tohoku-oki earthquake (hereafter, referred to as the Tohoku earthquake), M7 class interplate earthquakes, their afterslips (Suito et al., 2011), SSEs with repeating earthquakes and/or earthquake swarms (Uchida et al., 2016; Nishikawa et al., 2019; Honsho et al., 2019), and slow earthquakes (Nishikawa et al., 2019). In addition, remarkable slip behavior in the Tohoku subduction zone was L-ASE prior to the Tohoku earthquake (Yokota & Koketsu, 2015; Mavrommatis et al., 2015), which occurred from 2002 until the occurrence of the Tohoku earthquake in the downdip of rupture area of the Tohoku earthquake. The 2002 L-ASE provided stress accumulation in the rupture area of the Tohoku earthquake and was interpreted as a possible precursor to the large interplate earthquake. However, small-scale aseismic slips, such as SSEs, afterslips of M7 class earthquakes and L-ASE, after the Tohoku earthquake have not been well-investigated because of the evident postseismic deformation of the Tohoku earthquake (Iinuma et al., 2016; Tomita et al., 2020).

This study investigated small-scale aseismic slips using onshore Global Navigation Satellite Service (GNSS) sites after the 2011 Tohoku earthquake. Subsequently, afterslip distributions of M7 class interplate earthquakes and a possible L-ASE from late 2019 were reported. Considering these new findings, the slip behavior off Tohoku was discussed.

2 Data and Methods

2.1 Data and pre-processing

GNSS Earth Observation Network System (GEONET) F5 daily solutions for the East-West (EW), North-South (NS), and Up-Down (UD) components, which are distributed by Geospatial Information Authority of Japan (GSI) (Takamatsu et al., 2023), were employed as raw GNSS time-series data in this study. The data collection period was from March 12, 2011, to November 20, 2021. The employed observational sites were 213 GEONET sites, which have over 3000 daily solutions, were located within the latitudes of 36–42° and longitudes of 139–142° (Figure 1).

The raw GNSS data were considered to include the following factors: (a) postseismic deformation of the 2011 Tohoku-oki earthquake, (b) offsets due to earthquakes after the 2011 Tohoku-oki earthquake and GNSS antenna maintenance, (c) postseismic deformation of large earthquakes after the 2011 Tohoku-oki earthquake, (d) common mode error (CME), (e) periodic variation, and (f) other crustal deformation factors. The preprocessing method of this study excluded factors (a), (b), (d), and (e) to examine the afterslip of large earthquakes after the 2011 Tohoku-oki earthquake and other aseismic slip events. The earthquake catalog after the 2011 Tohoku-oki earthquake was obtained from the F-net earthquake catalog (Okada et al., 2004) at latitudes of 32–44°, longitudes of 136–148°, and magnitudes larger than 5.0. The preprocessing steps are as follows, and Figure 2 shows an example of the pre-processing results for the EW component of site 950167 (Yamada, Iwate prefecture).

First, the contributions of postseismic deformation due to the 2011 Tohoku-oki earthquake (a) were modeled. Postseismic deformation due to a large earthquake can be modeled by logarithm and/or exponential functions (e.g., Bevis & Brown, 2014). For modeling (a), it is preferable to employ a combination of two logarithmic functions and one exponential function (Fujiwara et al., 2022). Placing the raw GNSS time-series for the kth component of the nth site as $D_{n,k}^{\mathrm{raw}}(t)$ with time (days) of t, contributions (a) and (b) are modeled as follows:

$$D_{n,k}^{\mathrm{raw}}(t) = D_{n,k}^{\mathrm{ini}}(t) + \sum_{l=1}^{L_n} h_l H(t - t_l) + \epsilon_{n,k}(t) \quad (1)$$

with

$$D_{n,k}^{\mathrm{ini}}(t) = a_{n,k} + b_{n,k}t + c_{n,k}\log(1 + t/\tau_1) + d_{n,k}\log(1 + t/\tau_2) + e_{n,k}\left(1 - \exp(-t/\tau_3)\right) \quad (2)$$

where H is a Heaviside step function, τ_1, τ_2, and τ_3 are the relaxation times expressing the postseismic deformation of the 2011 Tohoku-oki earthquake ($\tau_1 = 1.59$, $\tau_2 = 148.6$, and $\tau_3 = 3645$ days; Fujiwara et al., 2022), and $\epsilon_{n,k}(t)$ indicates the residual time-series. t_l represents the day of occurrence of an offset event, and L_n represents the total number of offset events for the nth site. An earthquake with an epicenter within the threshold distance was considered an offset event. The threshold distance r_0 depends on the moment magnitude, as with Ikuta et al. (2012):

$$r_0 = \begin{cases} 10^{M_{\mathrm{w}}-4.3} & \text{if } M_{\mathrm{w}} \geq 6.8 \\ 10^{M_{\mathrm{w}}/2-0.9} & \text{if } M_{\mathrm{w}} < 6.8 \end{cases} \quad (3).$$

In addition, GNSS antenna maintenance was included as an offset event, which is listed in the maintenance table distributed by the GSI. The unknown parameters in Eqs. 1 and 2 ($a_{n,k}$, $b_{n,k}$, $c_{n,k}$, $d_{n,k}$, $e_{n,k}$, and h_l) were estimated using the least-squares method. When multiple offset events were detected within 3 d, these events were compiled as a single offset event, and the occurrence time of the compiled event was set as the earliest time among the events. The black and red curves show the raw and modeled time-series using Eq. 1 in Figure 2a.

Second, the contribution of the CME (d), which is a common bias among GNSS sites, was modeled by stacking detrended GNSS time-series (Widowinski et al., 1997). Here, Seasonal and Trend decomposition using Loess (STL) analysis (Cleveland et al., 1990) was performed to obtain the trend of the GNSS time-series as follows:

$$D_{n,k}^{\mathrm{raw}}(t) - D_{n,k}^{\mathrm{ini}}(t) = S_{n,k}(t) + T_{n,k}(t) + \epsilon_{n,k}(t) \quad (4)$$

where $S_{n,k}(t)$ and $T_{n,k}(t)$ are the seasonal and trend components, respectively. Then, the CME for each day $CME_k(t)$ was calculated as the 20% trimmed mean of $D_{n,k}^{\mathrm{raw}}(t) - D_{n,k}^{\mathrm{ini}}(t) - T_{n,k}(t)$ for a robust estimation. The gray and black plots in Figure 2b show the input time-series ($D_{n,k}^{\mathrm{raw}}(t) - D_{n,k}^{\mathrm{ini}}(t)$) and the time-series after removing the CMEs ($D_{n,k}^{\mathrm{raw}}(t) - D_{n,k}^{\mathrm{ini}}(t) - CME_k(t)$), respectively. The red curve in Figure 2b shows the trend component estimated by STL analysis.

Third, the contribution of offset events (b) was examined. Although the offset events were investigated in the first step, they included postseismic displacements and CMEs. To

extract pure offsets, the GNSS time-series after removing CME $D_{n,k}^{\mathrm{raw}}(t) - D_{n,k}^{\mathrm{ini}}(t) - CME_k(t)$ was divided into multiple time windows by the occurrence timings of the offset events, and the time-series for each time window was fitted by polynomial functions. The offset between two consecutive fitted time-series is the pure offset. For the polynomial functions, maximally 6-order of the polynomial function were employed, and the optimal order for each time window was determined by the AIC (Akaike's Information Criterion) value (Akaike, 1973). The red and orange curves in Figure 2c show the fitting curves of the polynomial functions and the offset time-series, respectively.

Fourth, the contributions of CMEs (d) and offset events (b) were re-examined because these contributions may affect each other; therefore, the second and third steps were repeated. Placing the calculated offset time-series in the third step as $O_{n,k}(t)$, the STL analysis was re-performed for $D_{n,k}^{\mathrm{raw}}(t) - D_{n,k}^{\mathrm{ini}}(t) - O_{n,k}(t)$, and the CMEs were re-obtained as $CME'_k(t)$ through the second step. Then, the third step was re-performed for $D_{n,k}^{\mathrm{raw}}(t) - D_{n,k}^{\mathrm{ini}}(t) - CME'_k(t)$, and the offset time-series was re-obtained as $O'_{n,k}(t)$.

Fifth, the contribution of the periodic variation (e) was examined using fast Independent Component Analysis (ICA) (Hyvarinen & Oja, 2000). Periodic variation is generally considered seasonal and has often been modeled by trigonometric functions with annual and semi-annual periods (Bevis & Brown, 2014). However, the seasonal variations are not necessarily stationary. Thus, this study handled the periodic components extracted from the fast ICA as periodic variations. Before performing the fast ICA, the other factors are maximally eliminated from the time-series in advance; here, the GNSS time-series $D_{n,k}^{\mathrm{raw}}(t) - D_{n,k}^{\mathrm{ini}}(t) - CME'_k(t) - O'_{n,k}(t)$ is modeled by the 8th order polynomial function and the exponential function following the occurrence of the earthquakes with the moment magnitude larger than 6.7 as:

$$D_{n,k}^{\mathrm{raw}}(t) - D_{n,k}^{\mathrm{ini}}(t) - CME'_k(t) - O'_{n,k}(t) = \sum_{i=0}^{8} f_{n,i} t^i + \sum_{l=1}^{L'_n} g_{n,l} \left[1 - \exp\left\{-\frac{t - t_l}{\tau'_l}\right\}\right] H(t - t_l) + \epsilon_{n,k}(t) \quad (5)$$

where L'_n is the total number of large earthquakes, and $f_{n,i}$ and $g_{n,l}$ are unknown parameters for this equation. Exponential functions correspond to the post-seismic deformation of large earthquakes. τ'_l is the relaxation time of the postseismic deformation for each large earthquake, which is given using the moment magnitude as $\tau'_l = 10^{M_{\mathrm{w}}-5.1}$. The relaxation time settings were determined through trial and error. The fast ICA was applied to the residual time-series $\epsilon_{n,k}(t)$ in Equation 5 for all components and all sites. Missing values in the residual time-series were interpolated by PPCA (probabilistic Principal Component Analysis) (Stacklies et al., 2007) before performing fast ICA. The results of the fast ICA with 20 independent components are shown in Figures S1 and S2. Assuming that the independent components of 1, 2, 4, 7, 8, 10, 12, 13, 14, 15, 18, and 19 demonstrated periodic variations, these components were summed. An example of the summated time-series is shown as a black plot in Figure 2d. Considering that the periodic variation should be continuous in time, the 3d Spline smoothing function was fitted to the summated time-series, as shown by the red curve in Figure 2d, and the smoothed time-series were handled as the periodic variation.

Sixth, the contributions of offset events (b) were re-examined by considering the above periodic variation. The third step was re-performed for $D_{n,k}^{\mathrm{raw}}(t) - D_{n,k}^{\mathrm{ini}}(t) - CME'_k(t) - P_{n,k}(t)$, and the offset time-series was re-obtained as $O''_{n,k}(t)$. where $P_{n,k}(t)$ are the periodic variations obtained in the fifth step. An example of the results estimated in this step is shown in Figure 2e. Moreover, a comparison between the estimated offsets and calculated displacements based on Global CMT solutions (Dziewonski et al., 1981; Ekström et al., 2012) assuming a uniform elastic half-space (Okada, 1992) is shown in Figures S3 and S4. As the estimated offsets and the calculated displacements are comparable with each other except the earthquakes on Jul. 10, 2011 and Oct. 25, 2013, the offsets were considered to be well obtained in this pre-processing. As the exceptional two earthquakes were relativel far-field events and provided similar displacements among the observational sites (Figures S3c and S3h), the coseismic signals might be removed as CME. These figures only show the results of the offset earthquake events, where the maximum calculated displacements are over 2.5 mm. Although the offsets were estimated for other earthquakes, the obtained offset displacements for those earthquakes generally showed random displacement fields, suggesting observational noise; thus, the estimated offsets for those events did not exceed the observational noise level and did not affect the trajectory modeling performed in the next section.

Finally, the pre-processed GNSS time-series $D_{n,k}(t)$ were obtained as $D_{n,k}(t) = D_{n,k}^{\mathrm{raw}}(t) - CME'_k(t) - O''_{n,k}(t) - P_{n,k}(t)$. An example of a pre-processed time-series is shown in Figure 2f.

2.2 GNSS site segmentation and trajectory modeling

Time-series stacking of multiple GNSS sites has often been conducted to suppress the effects of noise and highlight the effects of crustal deformation (e.g., Takagi et al., 2019). However, stacking too many sites may mask local crustal deformation. Here, segmentation of the GNSS sites was first conducted, and then averaging of the time-series for each segmented group was performed.

Before performing segmentation, the dominant contributions of the 2011 Tohoku-oki earthquake were removed by modeling $D_{n,k}(t)$ as $D_{n,k}^{\mathrm{post}}(t)$. $D_{n,k}^{\mathrm{post}}(t)$ has the same formula as that in Equation (2). An example of fitting by $D_{n,k}^{\mathrm{post}}(t)$ is shown by the red curve in Figure 2f, and the cumulative displacements due to $D_{n,k}^{\mathrm{post}}(t)$ are shown in Figure 3. Using the residual time-series, k-means cluster analysis was performed for segmentation. The total number of clusters was set to 18 so that the number of sites for each group was more than five. The latitude and longitude for each site were added to the end of the residual time-series in advance because spatially separated sites were determined to be in the same group without this process. The stacked time-series $D_{m,k}^{\mathrm{Stack}}(t)$ (m: the group number) was calculated as the average of the residual time-series and was obtained for each component of each group. The segmented groups and stacked time-series for each group are shown in Figures 4–6.

The stacked time-series were modeled by the following two approach, Model-1 and Model-2. The reasons why these two approaches were employed were discussed in Section 3.1. Model-1 includes the postseismic deformation of the 2011 Tohoku-oki earthquake, postseismic deformations due to large earthquakes with moment magnitudes larger than 6.7, and the 2011

and 2018 Boso SSEs (Ozawa et al., 2019). Although the stacked time-series already excluded the post-seismic deformation of the 2011 Tohoku-oki earthquake, it was also re-included considering its interaction with other factors. The 2014 Boso SSE also occurred in December 2013; however, its equivalent magnitude was relatively smaller than that of the 2011 and 2018 events so the displacements due to the 2014 event were not considered. Model-1 is given as follows:

$$D_{m,k}^{\text{Model}-1}(t) = D_{m,k}^{\text{Post}}(t) + \sum_{l=1}^{L'_m} g_{m,l}\left[1 - \exp\left\{-\frac{t-t_l}{\tau'_l}\right\}\right] H(t-t_l) + \sum_{j=1}^{J_m} h_{m,j}\hat{R}(t_j, T_j) \quad (6)$$

with

$$\hat{R}(t_j, T_j) = \frac{R(t_j)}{T_j} - \frac{R(t_j + T_j)}{T_j} \quad (7)$$

where $R(t)$ denotes the ramp function. The first term on the right-hand side represents the postseismic deformation of the 2011 Tohoku-oki earthquake, as shown in Equation 2: The second term on the right-hand side represents postseismic deformations due to large earthquakes with moment magnitudes greater than 6.7. The relaxation time τ'_l is given as $\tau'_l = 10^{M_w - 4.7}$ for the interplate earthquakes and $\tau'_l = 10^{M_w - 5.5}$ for the other types of earthquakes; the parameters for the index (4.7 and 5.5) were optimized to minimize the residuals of all groups. The third terms on the right-hand side represent the 2011 ($j = 1$) and 2018 ($j = 2$) Boso SSEs, where t_j and T_j are the onset time and duration of each SSE (Ozawa et al., 2019), respectively. This term was applied only to the southernmost group ($m = 8,16$).

Model-2 contains the 2019 L-ASE term in addition to Model-1 as:

$$D_{m,k}^{\text{Model}-2}(t) = D_{m,k}^{\text{Model}-1}(t) + q_m \hat{R}(t_{\text{LASE}}, T_{\text{LASE}}) \quad (8)$$

where t_{LASE} and T_{LASE} are the onset time and duration of the L-ASE, respectively. Because it is difficult to optimize the ending time of L-ASE, only t_{LASE} was optimized and determined to be November 25, 2019, by minimizing the residuals of all groups. This term was applied to all groups and T_{LASE} was set as the ending time corresponding to the end of the entire data period.

Then, to obtain displacements due to postseismic deformations following large earthquakes with moment magnitudes larger than 6.7, and the L-ASE for each site, Model-2 was also applied to the individual (not stacked) GNSS time-series for the kth component of the nth site as

$$D_{n,k}(t) = D_{n,k}^{\text{Model}-2}(t) + \epsilon_{n,k}(t) \quad (9).$$

2.3 Aseismic slip inversion method

To estimate the aseismic slip distributions, a geodetic slip inversion based on a non-negative least-squares method with Laplacian regularization was performed with the hyperparameter of regularization optimized by Akaike's Bayesian Information Criterion (ABIC)

(Akaike, 1980; Yabuki & Matsu'ura, 1992). Green's functions were obtained from the Green's function library for the Tohoku region, assuming a 3D elastic underground structure (Hori et al., 2021). The library expresses the plate interface by 3-dimensional B-spline functions, and the node points for the 3-dimensional B-spline functions are shown by gray circles in Figure 1. Zero-slip constraints for the southern, northern, and down-dip edges were also considered when providing Laplacian regularization (e.g., Zhou et al., 2014). The observational errors for the data covariance matrix assumed a diagonal matrix and the diagonal components were given as the model variances of the least-squares method in the trajectory modeling.

The slip inversion was performed for the afterslips of the major earthquakes (moment magnitude of 6.7 or greater) after 2012 and the 2019 L-SAE. Several large interplate earthquakes occurred in 2011. However, because large earthquakes occurred consecutively for the first 1 year after the 2011 Tohoku earthquake, the trajectory model failed to separately model the postseismic deformations of individual large earthquakes because of their trade-off relationship. Hence, these events were not examined in this study. Fully relaxed postseismic displacements, which were the coefficients of the exponential functions in Model-2, were employed as the input data for the inversion.

3 Results

3.1 Trajectory modeling of GNSS time-series

Figure 4b–d show stacked GNSS time-series for the individual site groups (Figure 4a) after the preprocess that eliminated postseismic deformation due to the 2011 Tohoku earthquake, offsets due to earthquakes and antenna maintenance, periodic variation, common mode errors, and constant plate motion from the raw GNSS time-series. While Figure 4 shows the results for site groups along the coastline, Figures 5 and 6 show those for the other groups.

The stacked GNSS time-series were firstly modeled by a combination of postseismic deformations of large earthquakes (moment magnitude of 6.7 or greater) and the 2011 and 2018 Boso SSEs using the trajectory fitting technique (Model-1, magenta curves in Figure 4b–d), which were modeled by exponential functions and ramp functions, respectively. The residuals of Model-1 for the horizontal components (magenta plots in Figure 4e–f) exhibited significant deviations from late 2019 to early 2021 in the central and southern Tohoku regions (Figures 4–6). Assuming that the deviation was driven by an unknown transient event, a ramp function was employed to model it, and its onset was estimated to be November 25, 2019. The ending time was set to the end of the data period because it was not properly optimized owing to the trade-off relationship with the postseismic deformations of the M7 class earthquakes on February 13, March 20, and May 1, 2021. The cyan curves in Figure 4b–d show the GNSS time-series modeled by Model-2, which considered the ramp function in addition to Model-1. Both Model-1 and Model-2 reproduced the observed GNSS time-series to a similar degree until the first half of 2019 (Figure 4e–f). Additionally, Model-2 successfully reproduced the time-series after late 2019 to a degree comparable to that of the former period. The dotted lines indicate 2σ error range of the Model-2 residuals, and it is confirmed that the deviation due to the transient movement in Model-1 was significant beyond the error range. The transient movement may be initiated gradually, unlike the ramp function; however, it is difficult to assess its initiation process considering data noises.

289

290 3.2 Slip distributions of the aseismic slip events

291 The black arrows in Figure 7a–c show the fully relaxed post-seismic horizontal
292 displacements of major interplate earthquakes with a moment magnitude of 6.7 or greater that
293 occurred after 2012. The vertical red and blue bars in Figure 8a–c show the fully relaxed post-
294 seismic vertical displacements. Figures 7a and 8a show the postseismic displacement fields of
295 M_w6.73 Sanriku-oki earthquake on February 16, 2015, and Figures 7b and 8b show those of
296 M_w6.81 Miyagi-oki earthquake on May 12, 2015. Figures 7c and 8c show the summation of the
297 postseismic displacement fields of the M_w7.10 Fukushima-oki (February 13, 2021), M_w7.06
298 Miyagi-oki (March 20, 2021), and M_w6.85 Miyagi-oki (May 1, 2021) earthquakes because the
299 contributions of these earthquakes were mixed owing to their trade-off relationship. Although the
300 first Fukushima-oki earthquake was an intraslab earthquake, the post-seismic deformations of the
301 later Miyagi-oki earthquakes were considered dominant because the displacements in Miyagi
302 (approximately N38.5°) were larger than those in Fukushima (approximately 37.5°N).

303 The postseismic displacements in Figures 7a–c are considered to demonstrate afterslip
304 because afterslip is a dominant process in postseismic deformation when the moment magnitude
305 of a mainshock is less than 7.5 (Sun & Wang, 2015). Therefore, afterslip distributions were
306 estimated from the post-seismic displacements using the geodetic slip inversion method in Figure
307 7a–c. As the results of the inversion, Figures 8a–c show the estimation errors, and Figures 8e–f
308 show the estimated slip over the 2σ estimation error for the inversion node points. The calculated
309 postseismic displacements are shown by blue arrows in the horizontal components (Figure 7a–c)
310 and by magenta and cyan bars (Figure 8a–c) in the vertical component. While the horizontal
311 calculated displacements largely fitted to the observations, the vertical calculated displacements
312 are much smaller than the observations. As the observed vertical displacements show spatially
313 random amounts, it is considered to be difficult to obtain the vertical postseismic displacements
314 by the trajectory modeling, because of the observational noises. Considering this matter, the
315 inversion results were mostly provided to explain the observed horizontal motions.

316 The afterslip of 2015 M_w6.73 Sanriku-oki earthquake was broadly estimated on the
317 shallow plate interface around N40° (Figure 7a), and the equivalent moment magnitude was
318 M_w7.17 (7.18×10^{19} Nm). This large moment release compared with the coseismic rupture
319 includes contributions from an SSE, which was reported by a seafloor geodetic and small
320 repeating earthquake study (Honsho et al., 2019) with a spatially compact slip of over 20 cm.
321 The estimated afterslip distribution may be oversmoothed by insufficient sensitivity to reproduce
322 shallow slip. The afterslip of the 2015 M_w6.81 Miyagi-oki earthquake was estimated to be in the
323 downdip portion of the mainshock (Figure 7b), and the equivalent moment magnitude was
324 M_w6.96 (3.50×10^{19} Nm). The cumulative afterslip of 2021 M_w7.06 and M_w6.85 Miyagi-oki
325 earthquakes was estimated in the downdip portion of the mainshocks (Figure 7c), and the
326 equivalent moment magnitude was M_w7.21 (8.12×10^{19} Nm). Although a slip was also
327 estimated at N40.5°, it could be artificial considering the estimation error (Figure 8g).

328 The black arrows in Figure 7d show the cumulative displacements modeled by the ramp
329 functions after November 25, 2019. The displacements generally demonstrated a trench-normal
330 direction, and the displacements along the eastern coastline were larger than those along the
331 back-arc area. Therefore, it is considered that this transient motion was driven by an L-ASE and
332 the slip distribution of this event was also estimated the geodetic inversion method. The

inversion results are summarized in Figures 7d, 8d, and 8h by the same manner with the other afterslip events in Figures 7 and 8. The slip distribution of this L-ASE event was estimated on the deep and shallow portions of the plate interface (Figure 7d), and the equivalent moment magnitude was M_w7.55 (2.67×10^{20} Nm). However, considering the estimation errors (Figure 8d and 8h), the shallow slip was insignificant. Moreover, a small-scale deep slip was estimated at the northernmost area around N41°, but it is difficult to guarantee its meaningfulness because artificial slips tend to occur at the edge of the analysis domain and because large displacements are not observed above this slip. Hence, this study only assessed the deeper aseismic slip of N37–39.5°N. The equivalent moment magnitude of the L-ASE is M_w7.35 (1.34×10^{20} Nm), and this event is consistent with the scaling law of seismic moment and duration (Ide et al., 2007) although the ending time of this event has currently not been well-identified.

4 Discussion

4.1 Spatial extent of L-ASEs

Various slip behaviors along Japan Trench (Nagai et al., 2001; Igarashi et al., 2001; Yamanaka & Kikuchi, 2003; Murotani et al., 2003; Yamanaka & Kikuchi, 2004; Iinuma et al., 2012; Yokota & Koketsu, 2015; Iinuma et al., 2016; Nakamura et al., 2016; Satake et al., 2017; Nishikawa et al., 2019; Nishimura, 2021) are summarized in Figure 9a, with the afterslips (blue contours) and the 2019 L-ASE (green countours) areas estimated in this study. The plate interface depth of the slip peaks of the 2019 L-ASE was approximately 60 km, which is deeper than that of any other slip phenomenon including the afterslip areas of the 2021 Miyagi-oki earthquakes. This depth corresponds to the depth at which aseismic slips are likely to occur due to the water supply (Nishikawa et al., 2023). As with the 2002 L-ASE (purple countours; Yokota & Koketsu, 2015), an obvious increase in seismicity was not observed at the initiation of the L-ASE, suggesting that the L-ASE spontaneously occurred where seismic activity could not appear. Because the estimated depth is greater than the downdip limit of interplate earthquakes (red dotted curve; Igarashi et al., 2001), the absence of seismicity at the initiation of the L-ASE supports the estimated depth.

Although the 2019 L-ASE was estimated to be in the downdip portion of the 2002 L-ASE, its spatial relationship remains controversial. The inversion results were not sufficiently sensitive to the shallower portion but demonstrated shallow slip (Figure 7d), which might suggest that the 2019 L-ASE possibly extended the shallower portion similar to the 2002 L-ASE. Moreover, spatial extent of the 2002 L-ASE includes M7 class earthquakes at the depth of approximately 20–40 km (e.g., Suito et al., 2011); the previous studies excluded postseismic deformations of those events (Yokota & Koketsu, 2015; Mavrommatis et al., 2015), the 2002 L-ASE distribution possibly included contributions of their afterslips and was estimated in the shallower portion. Considering these issues, it is difficult to determine whether the 2002 and 2019 L-ASEs were spatially complementary or overlapping. If they overlapped, the 2019 L-ASE may have been a recurring event in the 2002 L-ASE. Otherwise, the strains were released independently at different depths. In both cases, such an L-ASE is not a special event which occur just prior to the M9 megathrust earthquake but can occur even ~8 years after the M9 earthquake off Tohoku.

In the along-trench direction, the extent of L-ASE was determined to be better than that in the dip direction because of the site distribution (Figure 8d). In the northern and southern regions of the L-ASEs, deep aseismic slip events were found as afterslips of the Tohoku earthquake (cyan shaded region in Figure 9a; Iinuma et al., 2016) and repeated SSEs (green open circles in Figure 9a; Nishimura, 2021), respectively. Both the 2002 and 2019 L-ASEs compensated for deep aseismic slip in the along-trench direction and contributed to the release of strain at the deep plate interface.

4.2 Strain release process off Tohoku

Considering the locational uncertainty of the 2002 and 2019 L-ASEs, three cases of the strain release process associated with the L-ASEs have been suggested. Case-1: two spatially complementary slip domains exist, which are the very deep (2019 type) and deep (2002 type) L-ASEs and work individually (Figure 9b). Case-2: the very-deep L-ASE exists alone (Figure 9c); Case-3: the very-deep and deep L-ASEs work simultaneously (Figure 9d). The very-deep L-ASE exists independently of the other slips, whereas the deep L-ASE partially overlaps with medium-scale interplate earthquakes and their afterslips.

Assuming that both very-deep and deep L-ASEs occur repeatedly, they commonly have the following possible features, regardless of the above cases. First, slip rates of these L-ASEs (approximately 4 cm/yr and 6.5 cm/yr in this study and Yokota & Koketsu (2015), respectively) are lower than the maximum slip deficit rate (approximately 8 cm/yr), which suggests low strain accumulation rates during the inter-L-ASE period. Thus, partial or weak coupling due to the stress shadow of shallower locking may appear during the inter-L-ASE period. Second, L-ASEs may precede M7 class interplate earthquakes. This feature has already been suggested in an earthquake cycle simulation (Yokota & Koketsu, 2015). Actually, M7 class interplate earthquakes occurred after the initiation of the 2002 L-ASE (e.g., the 2005 August 16 Miyagi, 2008 May 8 Ibaraki, 2008 July 19 Fukushima earthquakes; magenta stars in Figure 9a), whereas no major earthquakes occurred during 1996–2002, and the 2021 Miyagi-oki earthquakes occurred after the initiation of the 2019 L-ASE. Additionally, it is well-known that M7 class earthquakes have repeatedly occurred in an interval of 30–40 years off Tohoku (e.g., Nakata et al., 2016), and conventional geodetic data suggest the possibility that onshore strain accumulation rates have temporal fluctuations with similar periodicity (Meneses-Gutierrez et al., 2022). These activities prior to 2002 were possibly triggered by the past L-ASEs. It was reported that SSEs promote intraslab earthquakes via water transportation in the Nankai subduction zone (Kita et al., 2021). Although intraslab earthquakes occurred following the 2002 and 2019 L-ASE (the 2003 May 26 Miyagi-oki earthquake, the 2021 Fukushima-oki earthquake, and the 2022 March 16 Fukushima-oki earthquake), the relationship between L-ASEs and intraslab earthquakes is beyond the range of this study, and it should be investigated carefully in the future. Finally, the L-ASEs are spatially complementary to the M9 rupture area; they contribute to enhancing stress accumulation in the M9 rupture area because Coulomb stress changes caused by an L-ASE promote stress accumulation in the updip portion of the L-ASE (Yokota & Koketsu, 2015).

Case-2 is the simplest scenario, in which a very-deep L-ASE occurs repeatedly, triggers M7 class earthquakes and their afterslips, and accumulates stress in the M9 rupture area. Case-3 indicates that the deep L-ASE also repeatedly occurs with the very deep L-ASE and has a similar

419 influence as in Case-2. However, the deep L-ASE collocates with the other slips; thus, the spatial
420 complexity of the deep plate interface and the interaction between the L-ASE and the collocated
421 slips should be considered. In Case-1, very deep and deep L-ASEs occur individually and
422 repeatedly, which affect the shallower plate interface, as in Cases 2 and 3. In addition to the
423 spatial complexity of the deep plate interface, the interaction between very deep and deep L-
424 ASEs should be considered. They may stimulate each other and occasionally occur
425 simultaneously. The most plausible senarios should be clarified in the future because these
426 scenarios would require different patterns of the frictional paramters on the plate interface. In
427 any case, note that the L-ASEs may stimulate various shallower slips and are possible precursors
428 of the entire M7 class and M9 seismicity.

429

430 **5 Conclusions**

431 This study processed the onshore GNSS data by the elaborated data-cleaning methods,
432 the stacking approach, and the trajectory modeling approach, and then revealed various small-
433 scale aseismic slip events (afterlips of M7-class earthquakes and an L-ASE since late 2019)
434 which had been hidden by a massive postseismic deformation of the 2011 M9 Tohoku
435 earthquake. The afterslip distributions of the 2015 M_w6.73 Sanriku-oki earthquake, the 2015
436 M_w6.81 Miyagi-oki earthquake, and the 2021 M7-class Miyagi-oki earthquakes and the slip
437 distribution of the 2019 L-ASE were estimated. The 2019 L-ASE is a similar event of the 2002
438 L-ASE (Yokota & Koketsu, 2015) prior to the 2011 M9 Tohoku-oki earthquake. The 2019 L-
439 ASE is considered to still be ongoing; if this event is the recurrence event of the 2002 L-ASE, its
440 duration would be over several years. The slip distribution of the 2019 L-ASE was estimated to
441 be on the deeper plate interface than any other slip behaviors including the 2002 L-ASE;
442 however, its possibly extended to the shallower portion as well as the 2002 L-ASE. This
443 locational uncertainty provides us various senarios of the repeatead occurrence of the L-ASEs off
444 Tohoku, but in any senarios, the L-ASEs may occur on the deep plate interface, promote M7-
445 class seismicity on the shallow plate interface, and provide strain accumulation in the M9 rupture
446 zone. Thus, it is important to monitor the ongoing L-ASE and seismicity and to assess the
447 interaction between L-ASEs and other slip behaviors through further numerical simulations in
448 the future.

449

450 **Acknowledgments**

451 I am thankful to the GSI for maintaining the GEONET sites and distributing the F5
452 solutions, Dr. Hiroaki Kobayashi for providing the slip distributions of the 2002 L-ASE and
453 afterslip of the 1994 Sanriku earthquake shown in Yokota & Koketsu (2015), and Dr. Ryoichiro
454 Agata for providing the Green's function library (Hori et al., 2021). The slip distributions of
455 major interplate earthquakes after the 2011 Tohoku earthquake (red contours in Figure 9a) using
456 strong-motion seismic waveform records were obtained from the Japan Meteorological Agency
457 webpage (https://www.data.jma.go.jp/eqev/data/sourceprocess/index.html) in Japanese. All
458 figures were drawn using Generic Mapping Tools (Wessel et al., 2013). This research was
459 supported by Japan Society for the Promotion of Science (JSPS) KAKENHI (Grant Number:
460 20K14588).

Open Research

The fully relaxed postseismic displacements of the 2015 Feb. 17, 2015 May 13, the 2021, earthquakes and the 2019 L-ASE displacements shown in Figures 7 and 8 are listed in Tables S1–4. Other data, such as grid files of slip distributions, are available from the authors upon reasonable request.

References

Akaike, H (1973), Information Theory and Maximum Likelihood Principle. In: Petrov BN, and Csäki F (Eds.) 2nd International Symposium on Information Theory. Akademiai Kiàdo, Budapest.

Akaike, H (1980), Likelihood and the Bayes procedure, In: Bernardo, J. M., DeGroot, M. H., Lindley, D. V., & Smith, A. F. M. (Eds.) Bayesian Statistics, 143–166, University Press, Valencia (1980).

Bevis, M., & Brown, A (2014), Trajectory models and reference frames for crustal motion geodesy. *J. Geod.*, *88*(3), 283–311. https://doi.org/10.1007/s00190-013-0685-5

Cleveland, R. B., Cleveland, WS, McRae, JE, & Terpenning, I (1990), STL: A seasonal-trend decomposition procedure based on loess. *J. Offic. Stat.*, *6*, 3–73.

Dziewonski, A. M., Chou, T. A., & Woodhouse, J. H (1981), Determination of earthquake source parameters from waveform data for studies of global and regional seismicity, *J. Geophys. Res.*, *86*, 2825–2852. https://doi.org/10.1029/JB086iB04p02825

Ekström, G., Nettles, M. & Dziewonski, A. M (2012), The global CMT project 2004-2010: Centroid-moment tensors for 13,017 earthquakes, *Phys. Earth Planet. Inter.*, *200–201*, 1–9. https://doi.org/10.1016/j.pepi.2012.04.002

Fujiwara, S., Tobita, M., & Ozawa, S (2022), Spatiotemporal functional modeling of postseismic deformations after the 2011 Tohoku-Oki earthquake. *Earth, Planets and Space*, *74*(1), 13. https://doi.org/10.1186/s40623-021-01568-0

Hirose, H., Asano, Y., Obara, K., Kimura, T., Matsuzawa, T., Tanaka, S., & Maeda, T (2010), Slow Earthquakes Linked Along Dip in the Nankai Subduction Zone. *Science*, *330*(6010), 1502. https://doi.org/10.1126/science.1197102

Honsho, C., Kido, M., Tomita, F., & Uchida, N (2019), Offshore Postseismic Deformation of the 2011 Tohoku Earthquake Revisited: Application of an Improved GPS-Acoustic Positioning Method Considering Horizontal Gradient of Sound Speed Structure. *J. Geophys. Res.*, *124*, 5990–6009. https://doi.org/10.1029/2018JB017135

Hori, T., Agata, R., Ichimura, T., Fujita, K., Yamaguchi, T., & Iinuma, T (2021), High-fidelity elastic Green's functions for subduction zone models consistent with the global standard geodetic reference system. *Earth Planets Space*, *73*, 41. https://doi.org/10.1186/s40623-021-01370-y

Hyvarinen, A. & Oja, E (2000), Independent Component Analysis: Algorithms and Applications, *Neural Networks*, *13*(4-5), 411–430. https://doi.org/10.1016/S0893-6080(00)00026-5

Ide, S., Beroza, G. C., Shelly, D. R., & Uchide, T (2007), A scaling law for slow earthquakes. *Nature*, *447*(7140), 76–79. https://doi.org/10.1038/nature05780

Igarashi, T., Matsuzawa, T., Umino, N., & Hasegawa, A (2001), Spatial distribution of focal mechanisms for interplate and intraplate earthquakes associated with the subducting Pacific plate beneath the

northeastern Japan arc: A triple-planed deep seismic zone, *J. Geophys. Res.*, *106*(B2), 2177-2191, https://doi.org/10.1029/2000JB900386

Iinuma, T., Hino, R., Kido, M., Inazu, D., Osada, Y., Ito, Y., Ohzono, M., Tsushima, H., Suzuki, S., Fujimoto, H., & Miura, S (2012), Coseismic slip distribution of the 2011 off the Pacific Coast of Tohoku Earthquake (M9.0) refined by means of seafloor geodetic data. *J. Geophys. Res.*, *117*, B07409. https://doi.org/10.1029/2012JB009186

Iinuma, T., Hino, R., Uchida, N., Nakamura, W., Kido, M., Osada, Y., & Miura, S (2016), Seafloor observations indicate spatial separation of coseismic and postseismic slips in the 2011 Tohoku earthquake. *Nat. Comm.*, *7*, 13506. https://doi.org/10.1038/ncomms13506

Ikuta, R., Satomura, M., Fujita, A., Shimada, S., & Ando, M (2012), A small persistent locked area associated with the 2011 Mw9.0 Tohoku-Oki earthquake, deduced from GPS data. *J. Geophys. Res.*, *117*, B11408. https://doi.org/10.1029/2012JB009335

Kita, S., Houston, H., Yabe, S., Tanaka, S., Asano, Y., Shibutani, T., & Suda, N (2021), Effects of episodic slow slip on seismicity and stress near a subduction-zone megathrust. *Nat. Comm.*, *12*(1), 7253. https://doi.org/10.1038/s41467-021-27453-8

Nagai, R., M. Kikuchi, & Y. Yamanaka (2001), Comparative study on the source processes of recurrent large earthquakes in Sanriku-oki Region: The 1968 Tokachi-oki earthquake and the 1994 Sanriku-oki earthquake, Zisin(2), *54*, 267-280. https://doi.org/10.4294/zisin1948.54.2_267

Nakamura, W., Uchida, N., & Matsuzawa, T (2016), Spatial distribution of the faulting types of small earthquakes around the 2011 Tohoku-oki earthquake: A comprehensive search using template events. *J. Geophys. Res.*, *121*, 2591–2607. https://doi.org/10.1002/2015JB012584

Nakata, R., Hyodo, M., & Hori, T (2012), Numerical simulation of afterslips and slow slip events that occurred in the same area in Hyuga-nada of southwest Japan. *Geophys. J. Int.*, *190*(2), 1213–1220. https://doi.org/10.1111/j.1365-246X.2012.05552.x

Nakata, R., Hori, T., Hyodo, M., & Ariyoshi, K (2016), Possible scenarios for occurrence of M~7 interplate earthquakes prior to and following the 2011 Tohoku-Oki earthquake based on numerical simulation. *Sci. Rep.*, *6*, 25704. https://doi.org/10.1038/srep25704

Nishikawa, T., Matsuzawa, T., Ohta, K., Uchida, N., Nishimura, T., & Ide, S (2019), The slow earthquake spectrum in the Japan Trench illuminated by the S-net seafloor observatories. *Science*, *365*(6455), 808–813. https://doi.org/10.1126/science.aax5618

Nishikawa, T., Ide, S., & Nishimura, T (2023), A review on slow earthquakes in the Japan Trench. *Progr. Ear. Planet. Sci.*, *10*(1), 1. https://doi.org/10.1186/s40645-022-00528-w

Nishimura, T (2021), Slow Slip Events in the Kanto and Tokai Regions of Central Japan Detected Using Global Navigation Satellite System Data During 1994–2020. *Geochem. Geophys. Geosys.*, ***22***(2), e2020GC009329. https://doi.org/https://doi.org/10.1029/2020GC009329

Mavrommatis, A. P., Segall, P., Uchida, N., & Johnson, K. M (2015), Long-term acceleration of aseismic slip preceding the Mw 9 Tohoku-oki earthquake: Constraints from repeating earthquakes. *Geophys. Res. Lett.*, *42*(22), 9717–9725. https://doi.org/10.1002/2015GL066069

Meneses-Gutierrez, A., Segall, P., & Sagiya, T (2022), How Steady is Interseismic Crustal Deformation in Northeast Japan? Evidence From an Integrated Analysis of Centennial Geodetic Data. *J. Geophys. Res.*, *127*(2), e2021JB023100. https://doi.org/https://doi.org/10.1029/2021JB023100

Miyazaki, S., Segall, P., Fukuda, J., & Kato, T (2004), Space time distribution of afterslip following the 2003 Tokachi-oki earthquake: Implications for variations in fault zone frictional properties. *Geophys. Res. Lett.*, *31*(6), L06623. https://doi.org/10.1029/2003gl019410

Murotani,T., Kikuchi,M., & Yamanaka, Y (2003), Rupture processesof large Fukushima-oki earthquakesin 1938., Abstract 2003 Japan Geoscience Union Meeting, S052-003.

Obara, K., & Kato, A (2016), Connecting slow earthquakes to huge earthquakes. *Science*, *353*(6296), 253–258. https://doi.org/10.1126/science.aaf1512.

Okada, Y (1992), Internal deformation due to shear and tensile faults in a half-space, *Bull. Seism. Soc. Am.*, *82*(2), 1018–1040. https://doi.org/10.1785/BSSA0820021018

Okada, Y., Kasahara, K., Hori, S., Obara, K., Sekiguchi, S., Fujiwara, H. & A. Yamamoto (2004), Recent progress of seismic observation networks in Japan –Hi-net, F-net, K-NET, and KiK-net–. *Earth Planet Space*, *56*, xv–xxviii. https://doi.org/10.1186/BF03353076

Ozawa, S., Yarai, H., & Kobayashi, T (2019), Recovery of the recurrence interval of Boso slow slip events in Japan. *Earth, Planets and Space*, *71*(1), 78. https://doi.org/10.1186/s40623-019-1058-y

Satake, K., Fujii, Y., & Yamaki, S (2017), Different depths of near-trench slips of the 1896 Sanriku and 2011 Tohoku earthquakes. *Geosci. Lett.*, *4*(1), 33. https://doi.org/10.1186/s40562-017-0099-y

Schwartz, S. Y., & Rokosky, J. M (2007), Slow slip events and seismic tremor at circum-pacific subduction zones. *Reviews of Geophysics*, *45*, 3. https://doi.org/10.1029/2006RG000208

Stacklies, W., Redestig, H., Scholz, M., Walther, D., & Selbig, J (2007), pcaMethods—a bioconductor package providing PCA methods for incomplete data, *Bioinformatics*, *23*, 9, 1164–1167. https://doi.org/10.1093/bioinformatics/btm069

Suito, H., Nishimura, T., Tobita, M., Imakiire, T., & Ozawa, S (2011), Interplate fault slip along the Japan Trench before the occurrence of the 2011 off the Pacific coast of Tohoku Earthquake as inferred from GPS data. *Earth, Planets and Space*, *63*(7), 19. https://doi.org/10.5047/eps.2011.06.053

Sun, T., & Wang, K (2015), Viscoelastic relaxation following subduction earthquakes and its effects on afterslip determination. *J. Geophys. Res.*, *120*(2), 1329–1344. https://doi.org/10.1002/2014JB011707

Takagi, R., Uchida, N., & Obara, K (2019), Along-Strike Variation and Migration of Long-Term Slow Slip Events in the Western Nankai Subduction Zone, Japan. *J. Geophys. Res.*, *124*(4), 3853–3880. https://doi.org/10.1029/2018JB016738

Takamatsu, N., Muramatsu, H., Abe, S., Hatanaka, Y., Furuya, T., Kakiage, Y., Ohashi, K., Kato, C., Ohno, K., & Kawamoto, S. (2023), New GEONET analysis strategy at GSI: daily coordinates of over 1300 GNSS CORS in Japan throughout the last quarter century. *Earth, Planets and Space*, *75*(1), 49. https://doi.org/10.1186/s40623-023-01787-7

Tomita, F., Iinuma, T., Ohta, Y., Hino, R., Kido, M., & Uchida, N (2020), Improvement on spatial resolution of a coseismic slip distribution using postseismic geodetic data through a viscoelastic inversion. *Earth, Planets and Space*, *72*(1), 84. https://doi.org/10.1186/s40623-020-01207-0

Tsang, L. L. H., Meltzner, A. J., Philibosian, B., Hill, E. M., Freymueller, J. T., & Sieh, K (2015), A 15 year slow-slip event on the Sunda megathrust offshore Sumatra. *Geophys. Res. Lett.*, *42*(16), 6630–6638. https://doi.org/https://doi.org/10.1002/2015GL064928

Uchida, N., Iinuma, T., Nadeau, R. M., Bürgmann, R., & Hino, R (2016), Periodic slowslip triggers megathrust zone earthquakes in northeastern Japan. *Science*, *351*(6272), 488–492. https://doi.org/10.1126/science.aad3108

Villegas-Lanza, J. C., Nocquet, J.-M., Rolandone, F., Vallée, M., Tavera, H., Bondoux, F., Tran, T., Martin, X., & Chlieh, M (2015), A mixed seismic–aseismic stress release episode in the Andean subduction zone. *Nat. Geosci.*, *9*(2), 150–154. https://doi.org/10.1038/ngeo2620

Wessel, P., W. H. F. Smith, R. Scharroo, J. Luis, & F. Wobbe (2013), Generic Mapping Tools: Improved Version Released, *EOS Trans. AGU*, *94*(45), 409–410. doi:10.1002/2013EO450001.

589 Widowinski, S., Bock, Y., Zhang, J., Fang, P., & Genrich, J (1997), Southern California Permanent GPS
590 Geodetic Array: Spatial filtering of daily positions for estimating coseismic and postseismic
591 displacements induced by the 1992 Landers earthquake, *J. Geophys. Res.*, *102*(B8), 18057–18070.
592 https://doi.org/10.1029/97JB01378

593 Yabuki, T., & Matsu'ura, M (1992), Geodetic data inversion using a Bayesian information criterion for
594 spatial distribution of fault slip. *Geophys. J. Int.*, *109*(2), 363–375. https://doi.org/10.1111/j.1365-
595 246X.1992.tb00102.x

596 Yamanaka, Y., & Kikuchi, M (2003), Source process of the recurrent Tokachi-oki earthquake on
597 September 26, 2003, inferred from teleseismic body waves. *Earth, Planets and Space*, *55*, 21–24.
598 https://doi.org/10.1186/BF03352479

599 Yamanaka, Y., & Kikuchi, M (2004), Asperity map along the subduction zone in northeastern Japan
600 inferred from regional seismic data, *J. Geophys. Res.*, *109*, B07307.
601 https://doi.org/10.1029/2003JB002683

602 Yokota, Y., & Koketsu, K (2015), A very long-term transient event preceding the 2011 Tohoku
603 earthquake. *Nat. Comm.*, *6*, 5934. https://doi.org/10.1038/ncomms6934

604 Zhou, X., Cambiotti, G., Sun, W., & Sabadini, R (2014), The coseismic slip distribution of a shallow
605 subduction fault constrained by prior information: the example of 2011 Tohoku (Mw 9.0)
606 megathrust earthquake. *Geophys. J. Int.*, *199*, 981–995. https://doi.org/10.1093/gji/ggu310
607

608

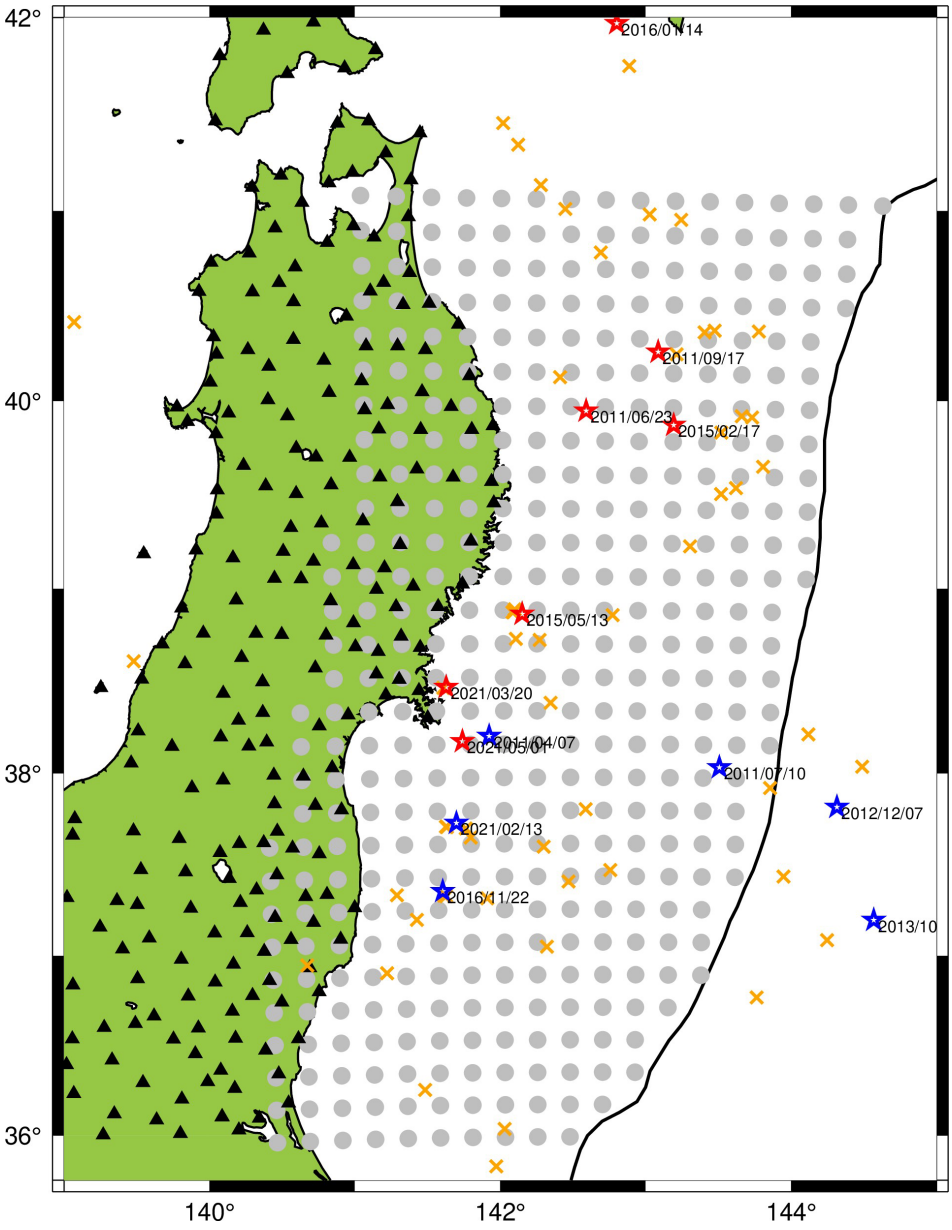

609

610 **Figure 1**. Black triangles show the GNSS sites used in this study. Gray circles show the 3d B-
611 spline nodes for Green's function library. Red and blue open stars show interplate and non-
612 interplate earthquakes with moment magnitudes of 6.7 and more, after the 2011 Tohoku
613 earthquake. Orange crosses indicate earthquakes with moment magnitudes between 6.5 and 6.7
614 after the 2011 Tohoku earthquake regardless of their mecanisms.

615

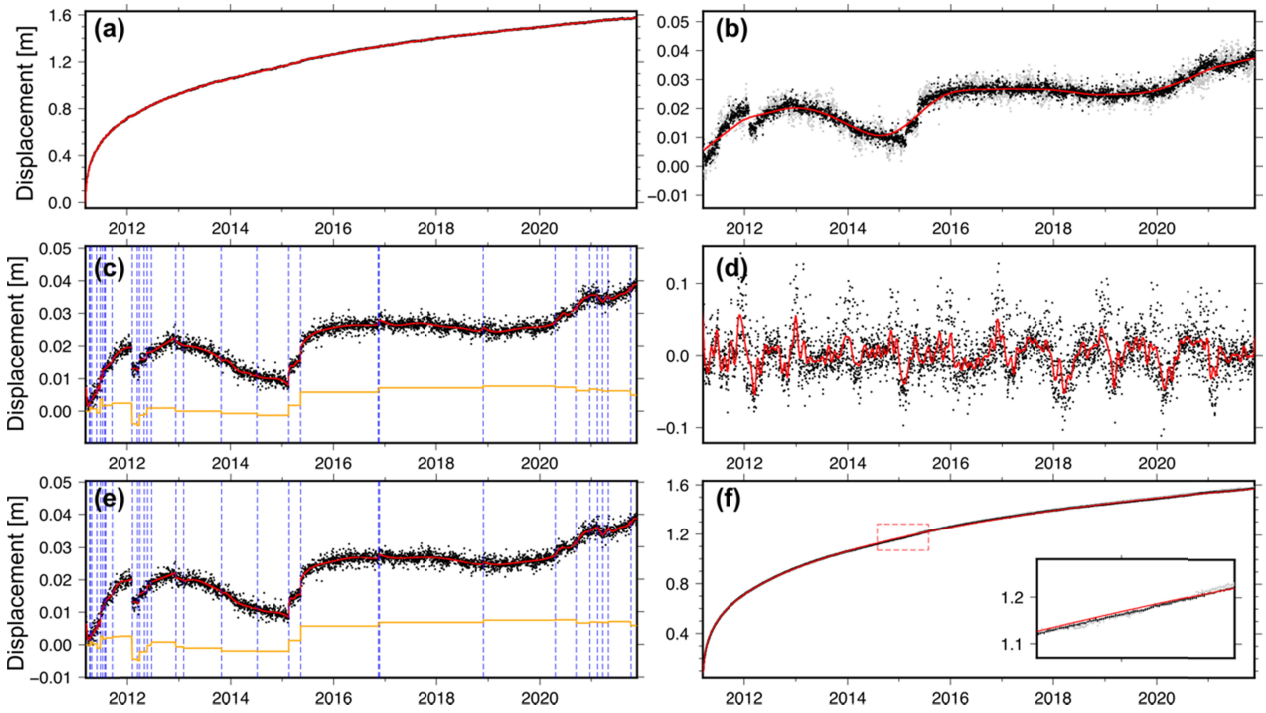

Figure 2. Example of GNSS pre-preprocessing in the EW component of the site 950167 (Yamada, Iwate Prefecture). The details of each panel are written in Section 2.1.

620

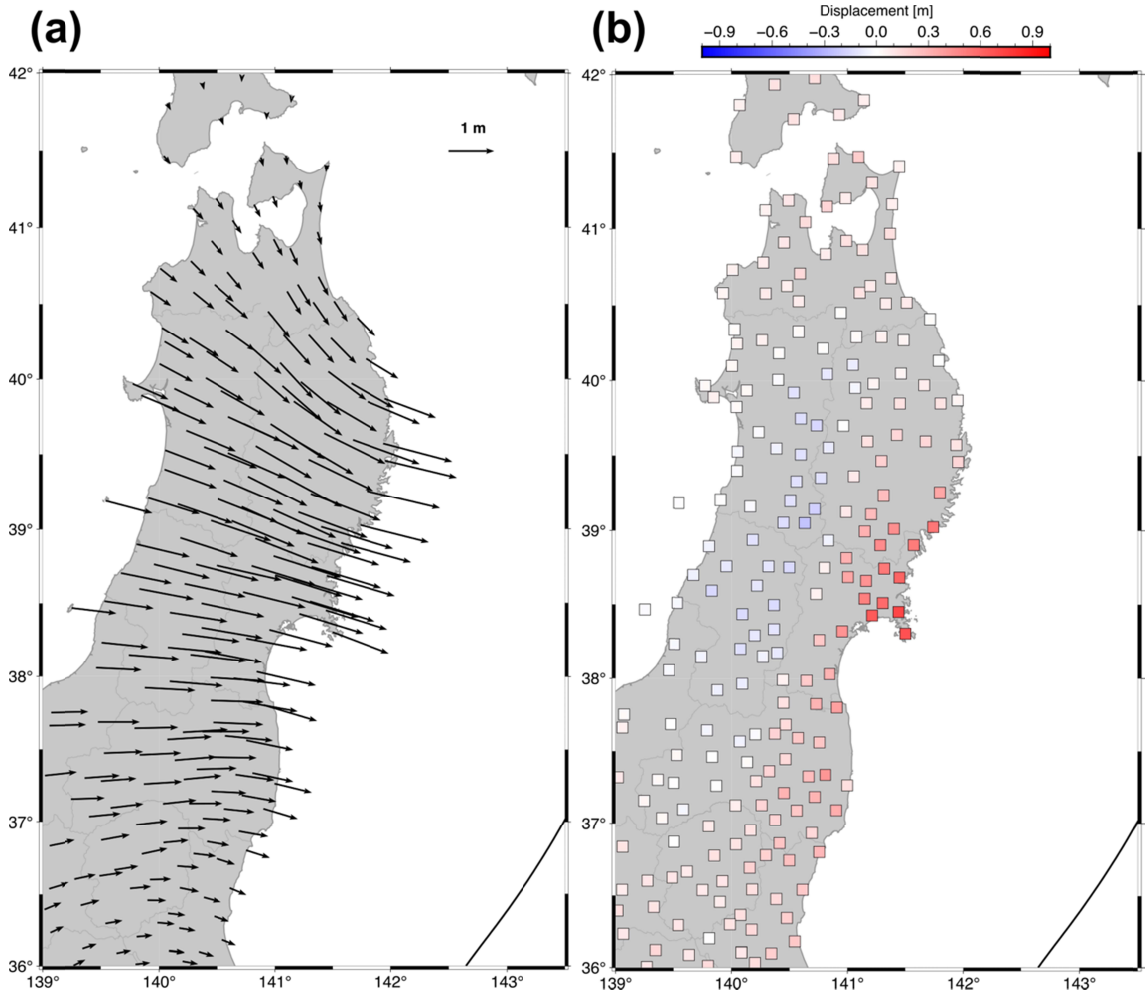

621

622 **Figure 3**. Cumulative post-seismic displacement associated with the 2011 Tohoku earthquake in
623 horizontal (a) and vertical (b) components. These displacements were calculated from Equation
624 (2) after the pre-processing.

625

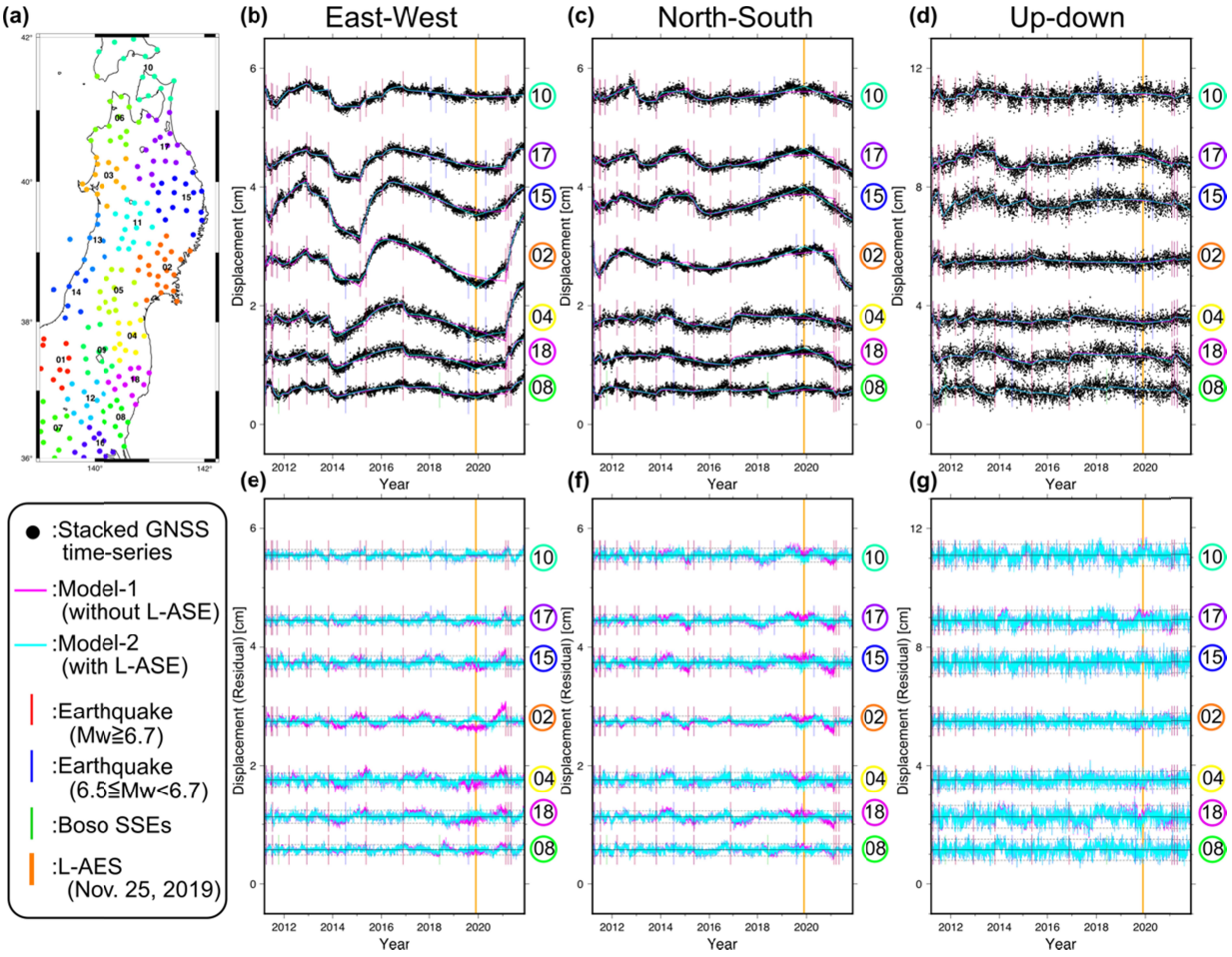

Figure 4. (a) GNSS site distribution. The colors indicate the site groups. (b–d) The stacked GNSS time-series after pre-processing for the site groups near the eastern coastline in EW, NS, and UD components. The magenta and cyan curves indicate the fitted curves of Model-1 and Model-2, respectively. The vertical red, blue, green, and orange lines show the timings of near-field earthquakes (Mw≧6.7), near-field earthquakes (6.5≦Mw＜6.7), the 2011 and 2018 Boso SSEs, and the 2019 L-ASE, respectively. (e–g) The residual GNSS time-series of Model-1 (magenta) and Model-2 (cyan). The other symbols are same with (b–d).

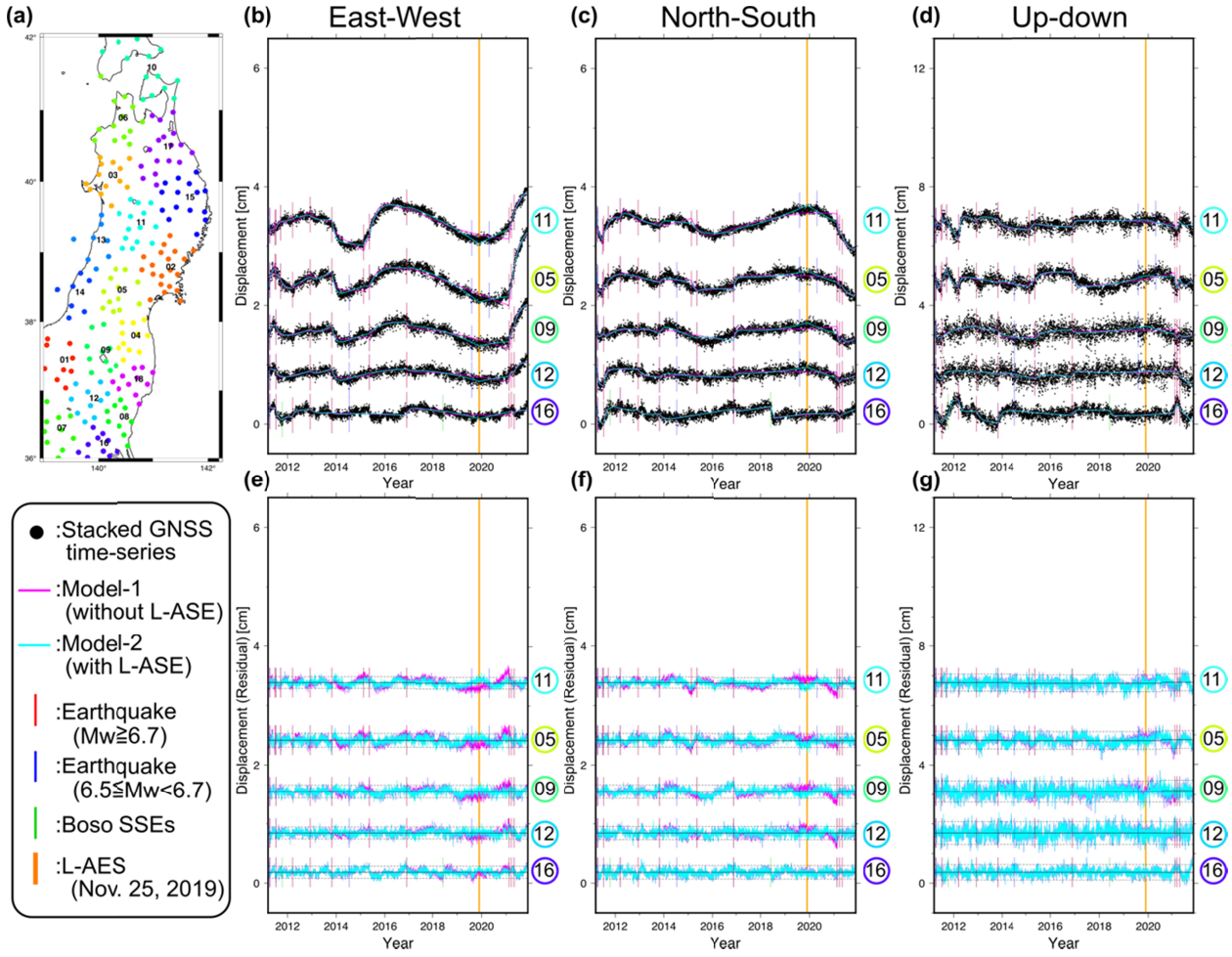

Figure 5. Stacked GNSS time-series for site groups in mid-Tohoku region. Symbols are shown in the same manner as in Figure 4.

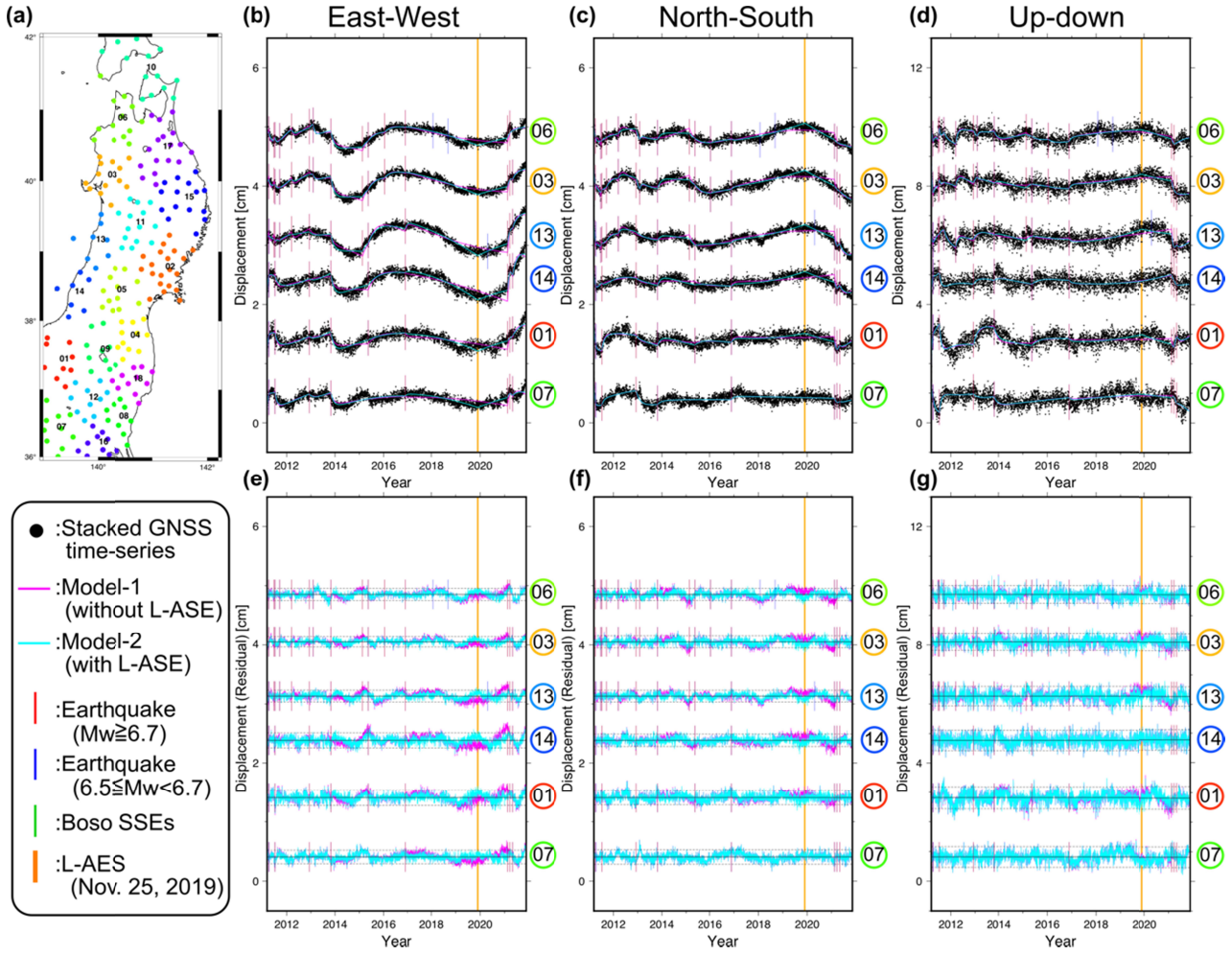

Figure 6. Stacked GNSS time-series for site groups along the western coastline. Symbols are shown in the same manner as in Figure 4.

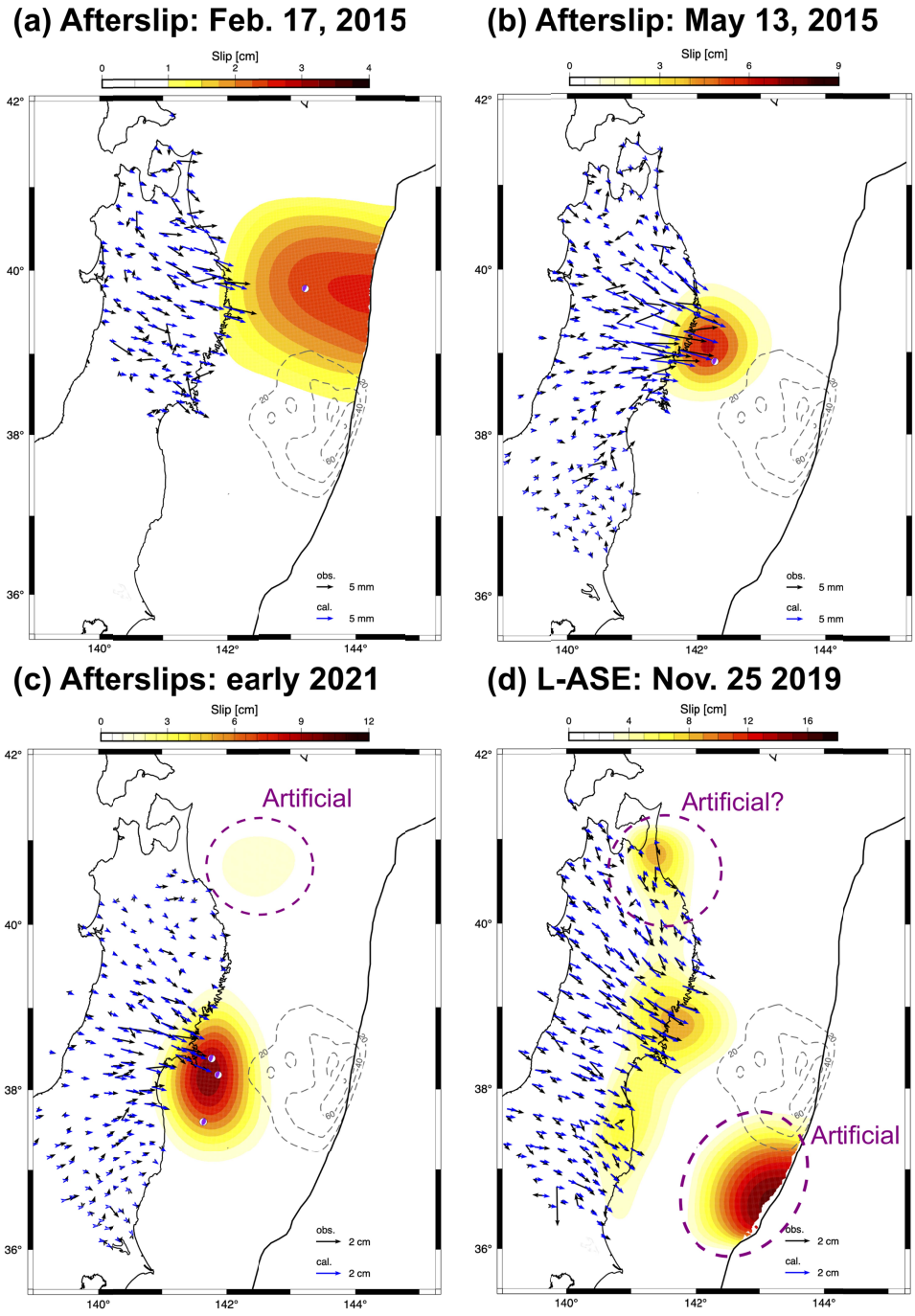

Figure 7. Color maps in (a)–(c) show the estimated afterslip distributions for the 2015 Feb. 17 Sanriku earthquake, the 2015 May 13 Miyagi earthquake, and the 2021 Mar. 20 and May 1 Miyagi earthquakes, respectively. The color map in (d) shows the estimated aseismic slip distribution of the 2019 L-ASE. The black and blue vectors show the observed and calculated cumulative displacements, respectively (displacements due to the 2021 Feb. 13 Fukushima earthquake are included in (c)). The mechanism solutions of the mainshocks are shown in (a)–(c). Dotted contours show the coseismic slip distribution of the 2011 Tohoku earthquake (Iinuma et al., 2012) with slip over 20 m.

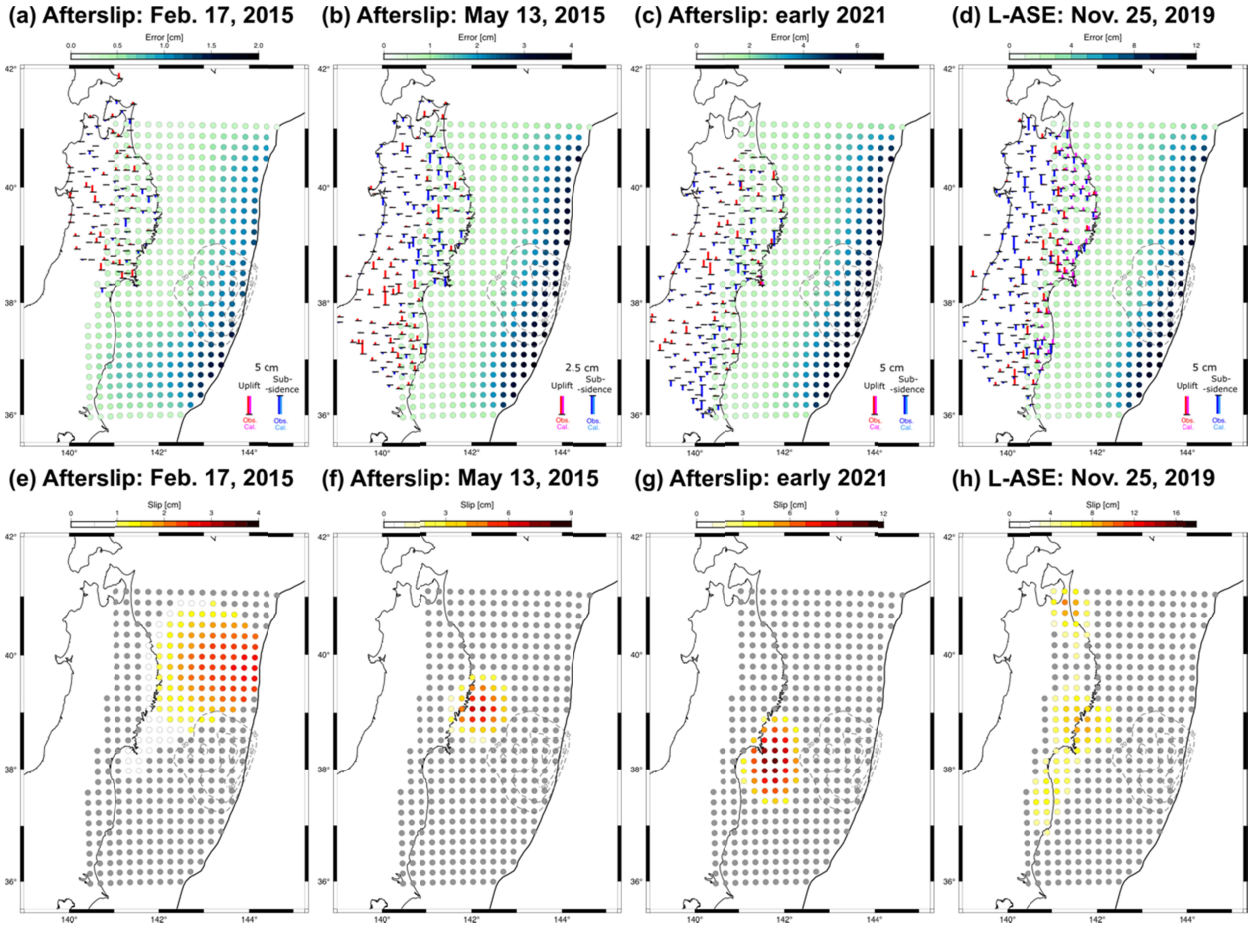

Figure 8. (a–d) Colored circles indicate the location of the 3d B-spline nodes of Green's function, and their colors indicate the estimation errors. The red and magenta vertical bars represent the observed and calculated uplift displacements, respectively, and the blue and cyan vertical bars represent the observed and calculated subsidence displacements, respectively. (e–h) The gray circles demonstrate the inversion nodes with the slip below 2σ estimation error, and the other colored circles demonstrate the inversion nodes with the significant slip over 2σ estimation error. The dotted contours in all panels indicate the co-seismic slip distribution of the 2011 Tohoku earthquake (Iinuma et al., 2012).

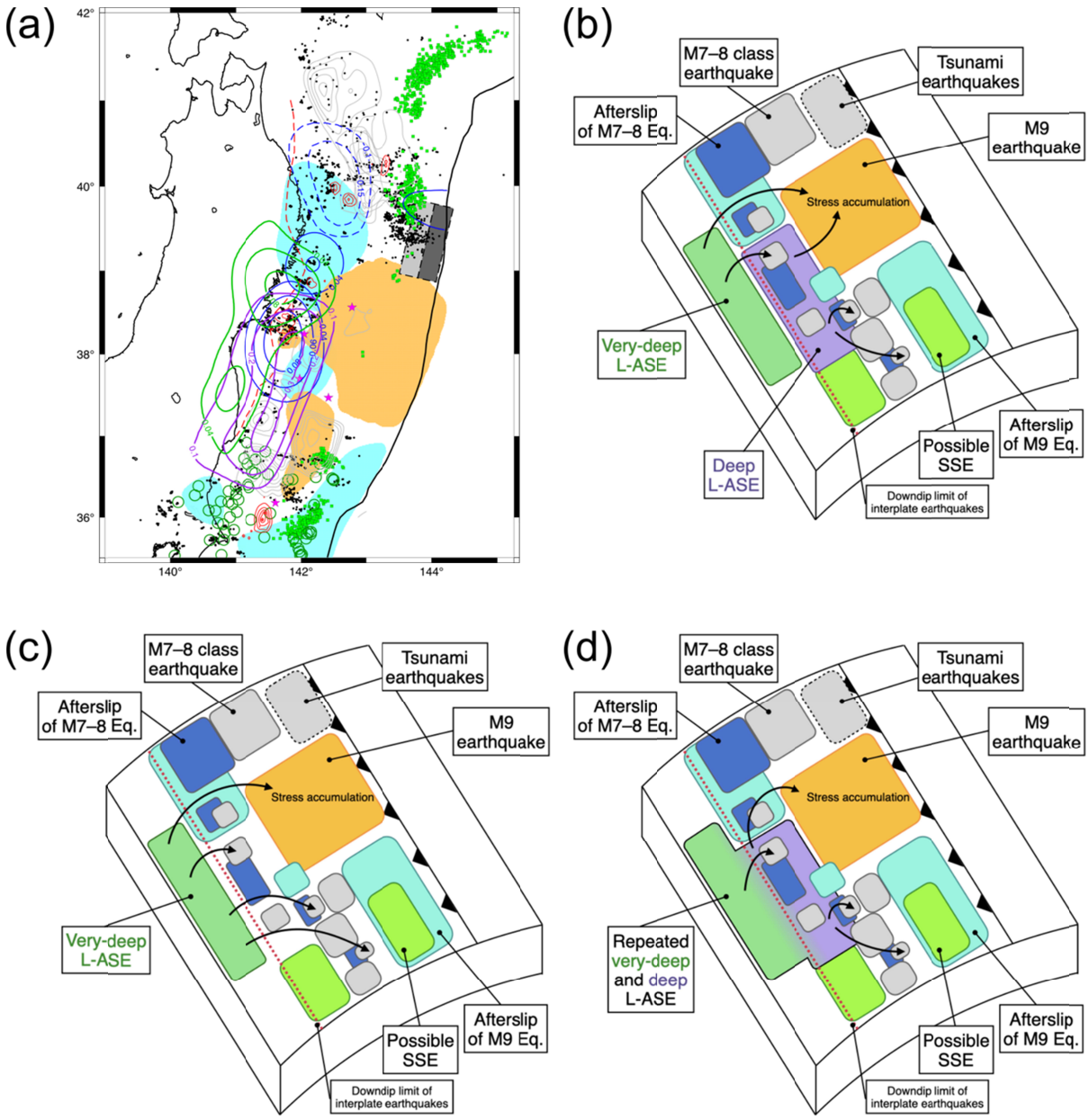

Figure 9. (a) Blue and green solid contours show the afterslip distributions and the 2019 L-ASE of this study, respectively. Orange and cyan shaded areas show the coseismic and afterslip areas of the 2011 Tohoku earthquake (Iinuma et al., 2012; Iinuma et al., 2016), respectively. Green squares and black dots demonstrate the tremors (Nishikawa et al., 2019) and the interplate earthquakes (Nakamura et al., 2016) after the 2011 Tohoku earthquake, respectively. Green open circles show the possible SSEs (Nishimura, 2021). Dark and light gray rectangles show the major tsunami sources of the 2011 Tohoku earthquake and the 1896 Meiji-Sanriku earthquake, respectively (Satake et al., 2017). Gray and red contours show the M7 class earthquakes before 2002 (Nagai et al., 2001; Murotani et al., 2003; Yamanaka & Kikuchi, 2003; Yamanaka & Kikuchi, 2004) and after 2011 Tohoku earthquakes (Japan Meteorological Agency solutions). Magenta stars show epicenters of M7 class earthquakes after 2002 until the 2011 Tohoku earthquake. Dotted blue and purple counters show afterslip of the 1994 Sanriku earthquake and

676 the 2002 L-ASE, respectively (Yokota & Koketsu, 2015). The red dotted curve indicates the
677 downdip limit of the interplate earthquakes (Igarashi et al., 2001). (b–d) Schematic images of the
678 possible scenarios associated with the L-ASEs.
679